2. RECENT EXPERIMENTAL STUDIES ON HEAT TRANSFER TO APOLLO COMMAND MODULE

By Robert A. Jones and James L. Hunt

SUMMARY

This paper presents some recent experimental results on the interference effects of protuberances and reaction-control jets on the heat transfer to the Apollo command module and some results of a basic investigation on the flow field and heat transfer in the separated region on the afterbody. The experiments were made in the Langley Mach 8 variable density tunnel which is a conventional blowdown facility. It was found that the presence of the shear pads increased the heat-transfer rate by factors as large as 2.5. Measurements of the separated-layer thickness on the afterbody indicate that this thickness varies with Reynolds number and is thicker at the lower Reynolds numbers. The heat transfer in the separated region was found to be a function of the separated-layer thickness. The results from several different types of ground facilities as well as some results from flight 1 of Project Fire were compared and it was found that an upper limit of heat transfer to the separated region could be defined.

INTRODUCTION

Although much research has been done on the heat transfer to the Apollo command module, several areas of uncertainty still exist. This paper will describe some recent experimental work related to two such areas. One is the interference effects of protuberances and reaction-control jets; the other is the heat transfer in the separated region on the afterbody. These studies were made in the Langley Mach 8 variable-density tunnel which is a conventional blowdown facility equipped with a model-injection mechanism for transient testing.

SYMBOLS

c_p specific heat at constant pressure

d diameter of face of model

H_t total enthalpy

h local measured heat-transfer coefficient

h_s heat-transfer coefficient at stagnation point

k thermal conductivity of model wall

M_∞ free-stream Mach number

p local measured pressure·

p_j stagnation pressure of reaction-control jet

p_t stagnation pressure behind normal shock at free-stream Mach number

$R_{\infty,d}$ free-stream Reynolds number based on body diameter

s surface distance

T_{aw} adiabatic wall temperature

T_{pc} phase-change temperature

T_t total temperature

u velocity at edge of separated boundary layer based on a reference temperature

z_t compressibility factor at stagnation conditions

α angle of attack; thermal diffusivity

δ separated-layer thickness measured normal to free-stream flow direction

μ viscosity based on reference temperature conditions at edge of separated boundary layer

ρ density based on reference temperature condition at edge of separated boundary layer

PROTUBERANCES AND REACTION CONTROLS

Photographs of the 0.026-scale model showing many of the protuberances are shown in figure 1. The effects of these irregularities on the heat transfer are difficult to measure by conventional thin-skin calorimeter techniques because of the small size of the models which can be tested in hypersonic facilities. The small models make instrumentation with thermocouples difficult and, in addition, since it is not known beforehand which area will be most affected it is difficult to determine where thermocouples should be placed.

To overcome these difficulties a new experimental technique developed at the Langley Research Center was used in the present study. This technique employs a very thin coating of a material which undergoes a visible phase change from an opaque solid to a clear liquid at accurately known temperatures. The model, which is made from a dark-colored low-thermal-conductivity plastic, is sprayed with just enough of this material to fog its surface. This coating, which has the appearance of tiny opaque white crystals, is less than 0.001 inch thick. The cool coated model is suddenly exposed to the test stream and the progression of the phase-change patterns is recorded by a time-study motion-picture camera. The temperature of the model surface at the location of the phase-change lines is assumed to be the same as the melting temperature of the particular material used. A photograph of the tunnel test section showing the model, camera, and stroboscopic flash light used to illuminate the model is presented in figure 2.

The isothermal-coated model is placed in the model injection mechanism located directly beneath the test section; the tunnel is then started and brought to the desired test condition; the camera and light are then turned on; and the model is rapidly injected into the test airstream. The useful test time is usually from 1/2 to 10 seconds. After completion of the test, the model is removed, the coating is washed off with a special thinner, and then the model is cooled and repainted for the next test. The value of the heat-transfer coefficient is found by relating the time elapsed, from model exposure until a particular phase-change pattern occurs, to the solution of the transient heat-conduction equation. One form of this solution is plotted in figure 3. The values of the model thermal properties k and α are known as well as the value of the temperature ratio T_{pc}/T_{aw}; thus for the time corresponding to any particular phase-change pattern, the heat-transfer coefficient can be read from this plot. A more complete description of this technique and a discussion of the accuracy obtainable with it is given in reference 1.

Prints of three individual frames of the motion-picture film taken during one test to determine heating rates in the vicinity of the shear pads on the face are given in figure 4. The lines separating the light and dark portion are lines at which the phase change is taking place and consequently are lines of known constant heat-transfer coefficient. Figure 5 is a map of the heat-transfer distribution on the face of the model showing the effects of the shear pads and tension ties. The maximum heating rates near the windward pads were 1.17 times the stagnation-point value. Measurements made in the same region on a smooth model indicate that the interference effect of the shear pads was to increase the heating rate by factors as large as 2.5.

Figure 6 shows photographs of the phase-change patterns near one of the reaction-control jets and a map of the heat-transfer distribution obtained from such patterns is given in figure 7. This reaction-control jet is located in what is normally the separated afterbody region. In figure 6 the thrust of the jet is outward so as to roll the top of the model away from the observer. The jet is a small contoured supersonic nozzle exhausting cool dry air. The design of this nozzle and the pressure at which it was operated were such as to match the exhaust expansion boundary of the reaction-control motors on the actual command module. The maximum heat-transfer coefficient measured in the interference region of the jet was 0.15 of the stagnation-point value which

corresponds to an increase of about 11 times the heating rate in the same area with the jet off. This increase in heating rate is rather large; however, during entry the control jets are fired in short bursts and during a portion of the trajectory which does not coincide with peak heating. Therefore, this increase in heating due to the control jet does not greatly affect the heat-shield design. Perhaps of more concern is the effect of the control jets on the afterbody pressure distribution and the resulting changes in net force caused by the jets. The regions of increased pressure should correspond roughly to the regions of increased heating; therefore the present technique may be of use in pressure-distribution studies.

The results discussed here as to the effects of protuberances and reaction controls on heat transfer are typical of the more complete results presented in reference 2.

SEPARATED AFTERBODY HEAT TRANSFER

Most of the data obtained in the separated region on the afterbody were obtained by using sting- or strut-mounted models which, of course, disturb the afterbody flow field and make interpretation of data difficult. In addition, no adequate theories or correlations for heat transfer in separated afterbody regions exist at the present time. Therefore a study of the flow field, pressure distribution, and heat transfer in the separated afterbody region was made.

Measurements of the separated-layer thickness at zero angle of attack are shown in figure 8 for two different model-support configurations. The technique used to make these measurements is illustrated in figure 9. A cylinder of approximately 1/16-inch diameter was coated with a temperature-sensitive material and placed in a hole in the afterbody surface so that it projected normal to the surface. When the model was exposed to the test airstream, the impingement of the separated shear layer on the coated cylinder resulted in a clearly defined phase-change pattern which indicated the position of the shear layer. Only one cylinder was used for each test, but by varying the location of this cylinder in subsequent tests, the streamlines of the shear layer shown in figure 8 were determined. The effect of the cylinder itself on the separated-layer thickness was thought to be negligible inasmuch as it had an insignificant effect on the measured afterbody pressure.

There are two interesting results indicated by the patterns of figure 8: (1) the separated-layer thickness varies with Reynolds number, the thicker layer occurring at the lowest Reynolds number, and (2) the separated-layer thickness varies with the sting or strut used to support the model. In all, four different strut configurations were studied. Two of these are shown in figure 8. The other two struts used consisted of a sting projecting straight back parallel to the center line of the model and one similar to the strut on the left in figure 8 except that it was twice as thick. The strut shown on the left of figure 8 appeared to have the least interference effect on the separated afterbody flow for zero angle of attack.

Measurements of the separated-layer thickness at an angle of attack of 35° are shown in figure 10. The separated-layer thickness is much larger than that for an angle of attack of 0° and a general trend for thicker separated layers at the lower Reynolds numbers is evident. The reversal of this trend at the two highest Reynolds numbers is not understood.

Figure 11 shows measured pressure distributions in the separated afterbody region for $\alpha = 0^\circ$ and 35°. These measurements were made with miniaturized thermocouple-type gages which were located inside the model and connected to the orifices with 1/2-inch lengths of tubing. These gages responded very rapidly and less than 1 second was required for a measurement; thus, the model remained near room temperature. For both angles of attack the level of pressure varies with Reynolds number; the higher pressures occur at the lower Reynolds numbers. This trend is similar to the variation in separated-layer thickness where the thicker layers occurred at the lower Reynolds number. Calculations of the afterbody pressure made by assuming that the flow expands isentropically from stagnation conditions around to the measured separation angle were in close agreement with the measured pressure levels for an angle of attack of 0°.

Several attempts were made to correlate the heat transfer to the separated afterbody by using the measured separated-layer thickness and pressures discussed earlier. One possible correlation is shown in figure 12 for an angle of attack of 0°. In this figure the Stanton number based on local flow conditions external to the separated boundary layer is plotted as a function of the ratio of surface distance from the rear of the afterbody to the separated-layer thickness measured normal to the free-stream flow direction. The measured heat-transfer coefficients were taken from reference 3 which describes a heat-transfer study for the afterbody of this same configuration which was also made in the same facility under similar test conditions. The different symbols denote Reynolds numbers in the same manner as for figure 11. Although the correlation of figure 12 is for a limited range of conditions, it does indicate that the heat-transfer rate in the separated afterbody region is sensitive to the separated-layer thickness which, in turn, is a function of Reynolds number as well as of the sting or strut configuration used in the test.

In view of the fact that the afterbody separated flow field is affected by the model support, extrapolation of ground-facility results to flight conditions is difficult. However, by comparing data obtained in several different facilities under different test conditions, an upper limit for heat transfer to this region can be defined. Figure 13 shows data from several facilities as well as data from flight 1 of Project Fire. These data are presented in terms of a local Stanton number based on conditions at the edge of the separated boundary layer as a function of local Reynolds number based on the same conditions and surface distance from the forward stagnation point. For most of these data, the local conditions were determined by expanding the flow isentropically from stagnation conditions to the measured afterbody pressure. In cases where the afterbody pressures were not available, correlations were used to determine the pressure. The set of data points for the Project Fire high-altitude case were handled somewhat differently. At these flight conditions the flow around the body is in chemical nonequilibrium; thus, in order to get the local Stanton

UNCLASSIFIED

numbers, the composition was assumed to be frozen at the stagnation equilibrium conditions and expanded isentropically to the measured afterbody pressure.

It can be seen in figure 13 that a line representing the upper limit of these different data can be drawn. Such a line would correspond to approximately 5 percent of the calculated convective heat-transfer rate for the stagnation point at an angle of attack of $0°$ and could be used as an upper limit for heat-shield design.

A comparison of the afterbody pressure data obtained during flight 1 of Project Fire with the afterbody pressures of the present study is given in figure 14. For the low Reynolds number flight data, the band shown represents the scatter in the telemetered data. There were no pressure data obtained in flight for the Reynolds number range between the points shown since the high dynamic pressure drove the gages off scale. This comparison indicates that much the same variation of afterbody pressure with Reynolds number occurred even though the test conditions were very different.

CONCLUDING REMARKS

In concluding, it is necessary to point out that although the new experimental techniques described herein have obtained test results which are helpful in determining the Apollo heat-shield design, these data were obtained under conditions far different from those that will be encountered during the Apollo reentry. Therefore, data from flights such as Fire, Mercury, Gemini, and the early earth-orbital Apollo flights must be carefully analyzed and used for confirmation of the design.

REFERENCES

1. Jones, Robert A.; and Hunt, James L.: An Improved Technique for Obtaining Quantitative Aerodynamic Heat-Transfer Data With Surface Coating Materials. Paper No. 65-131, Am. Inst. Aeron. Astronaut., Jan. 1965.

2. Jones, Robert A.; and Hunt, James L.: Effects of Cavities, Protuberances, and Reaction-Control Jets on Heat Transfer to the Apollo Command Module. NASA TM X-1063, 1965.

3. Jones, Robert A.: Experimental Investigation of the Overall Pressure Distribution, Flow Field, and Afterbody Heat-Transfer Distribution of an Apollo Reentry Configuration at a Mach Number of 8. NASA TM X-813, 1963. (Supersedes NASA TM X-699.)
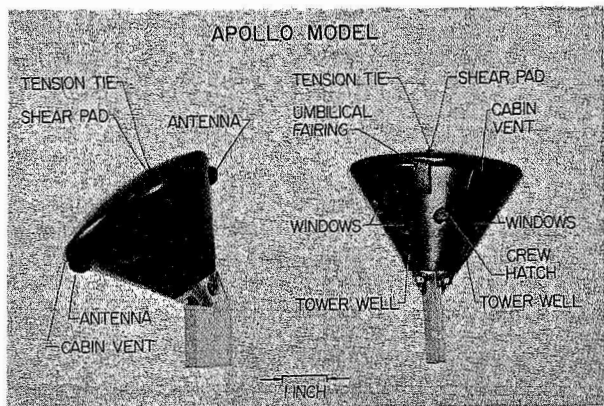
UNCLASSIFIED
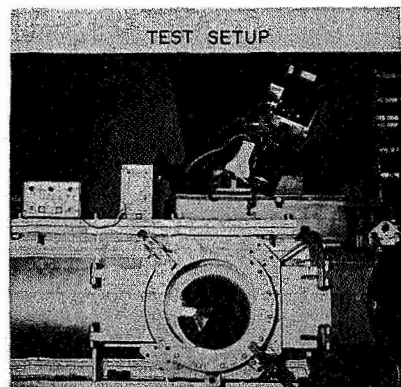
Figure 1

L-2458-1

Figure 2

L-2458-2
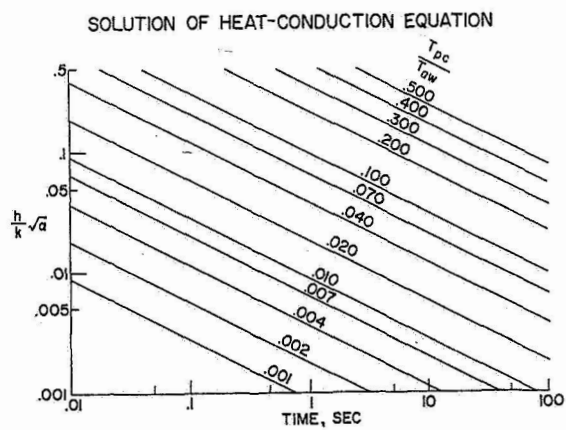
Figure 3
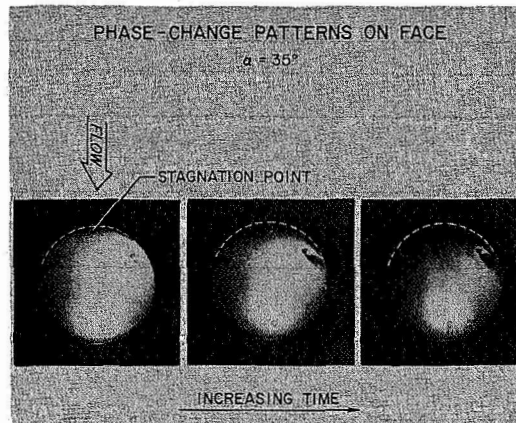
Figure 4

L-2458-4

HEAT-TRANSFER MAP OF FACE

h/h_s

Figure 5

PHASE-CHANGE PATTERNS OF REACTION-CONTROL JET

$\alpha = 35°$

FLOW

INCREASING TIME

Figure 6   L-2458-6

HEAT-TRANSFER MAP OF REACTION-CONTROL JET

$R_{\infty,d} = 0.13 \times 10^6$; $p_j/p_t = 606$; $\alpha = 35°$

LEEWARD RAY

WINDWARD RAY   WINDWARD RAY

h/h_s

.15

.12

.08

.12

Figure 7

SEPARATED-LAYER THICKNESS

$\alpha = 0°$

$R_{\infty,d}$ $R_{\infty,d}$

.1 × 10⁶   .1 × 10⁶

.2 × 10⁶   .2 × 10⁶

.5 × 10⁶   .5 × 10⁶

1.4 × 10⁶   1.4 × 10⁶

FLOW
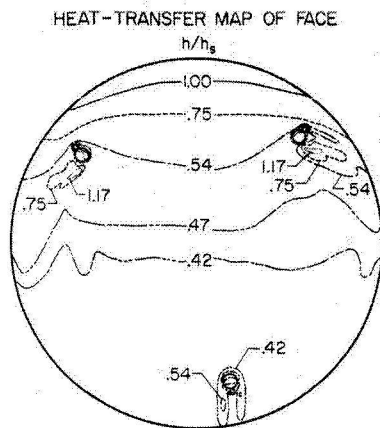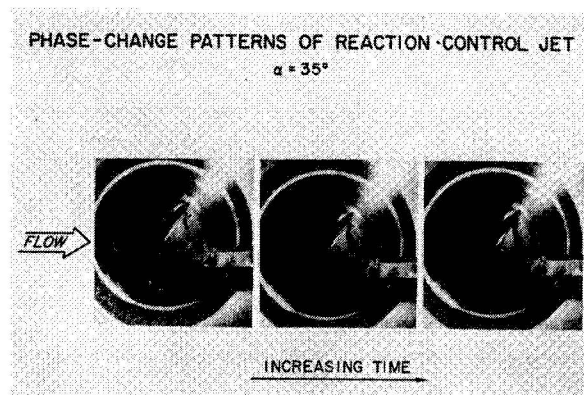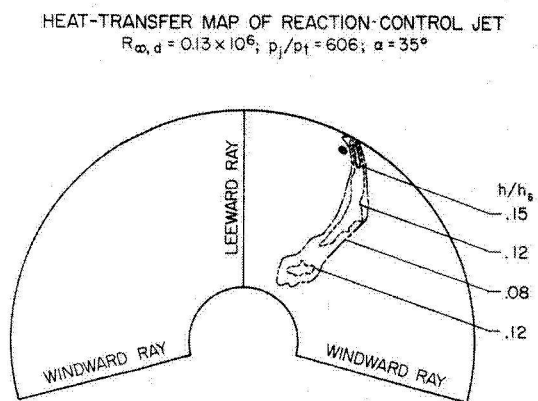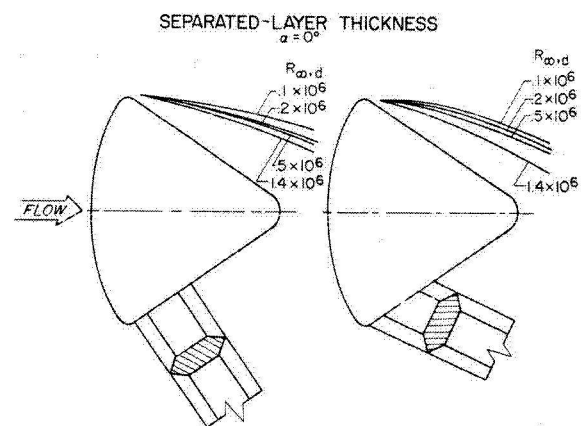
Figure 8

TECHNIQUE FOR MEASURING SEPARATED-LAYER THICKNESS
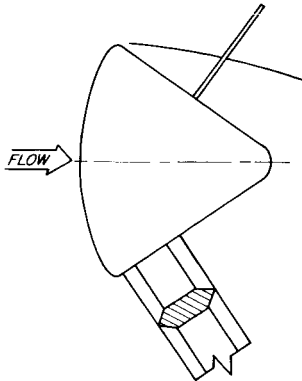
Figure 9

SEPARATED-LAYER THICKNESS
$\alpha = 35°$
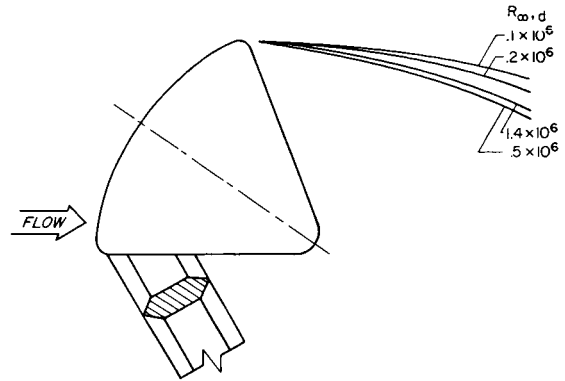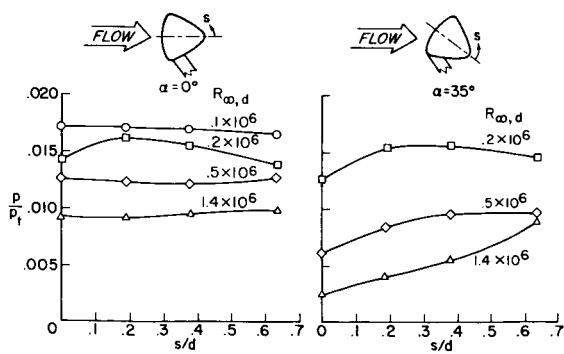

Figure 10

AFTERBODY PRESSURE DISTRIBUTIONS

Figure 11
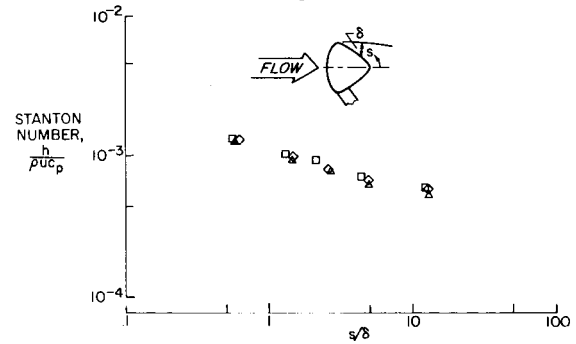
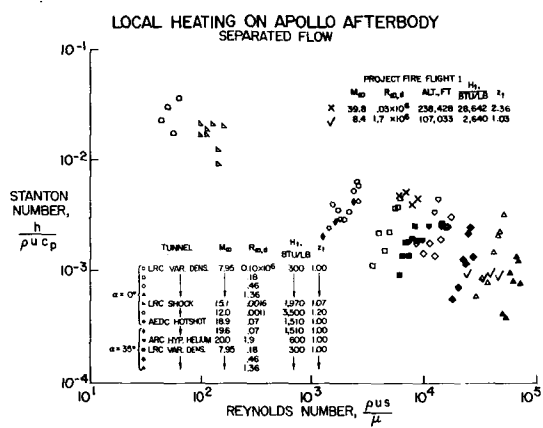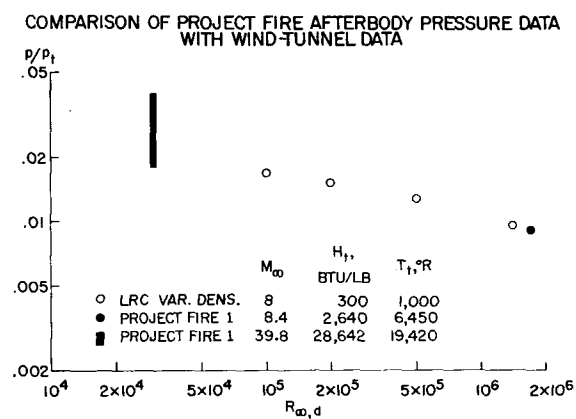HEAT-TRANSFER DISTRIBUTION ON AFTERBODY
$\alpha = 0°$

Figure 12

LOCAL HEATING ON APOLLO AFTERBODY
SEPARATED FLOW

Figure 13

COMPARISON OF PROJECT FIRE AFTERBODY PRESSURE DATA WITH WIND-TUNNEL DATA

Figure 14